proteasome activity and its inhibition chemistry. The insights into the atomic details of the catalytic center of the human 20S proteasome—an actual target of cancer therapeutics—provide important clues for the design of a new class of proteasome inhibitors. In particular, our results suggest that dual-electrophile inhibitors, where both electrophiles are in a β position to each other, would exhibit kinetically enhanced inhibition rates. Generally, with the tools described here, large numbers of such potential cancer therapeutics can be structurally analyzed at high resolution (several hundred per week could be feasible in an industrial setting), allowing for systematic exploration of ligand binding space toward improved efficacy and specificity.

REFERENCES AND NOTES

1. M. Bochtler, L. Ditzel, M. Groll, C. Hartmann, R. Huber, *Annu. Rev. Biophys. Biomol. Struct.* **28**, 295–317 (1999).
2. E. Kish-Trier, C. P. Hill, *Annu Rev Biophys* **42**, 29–49 (2013).
3. A. Ciechanover, *Cell* **79**, 13–21 (1994).
4. D. Finley, *Annu. Rev. Biochem.* **78**, 477–513 (2009).
5. M. Groll et al., *Nature* **386**, 463–471 (1997).
6. W. Harshbarger, C. Miller, C. Diedrich, J. Sacchettini, *Structure* **23**, 418–424 (2015).
7. P. C. da Fonseca, E. P. Morris, *Nat. Commun.* **6**, 7573 (2015).
8. A. Chari et al., *Nat. Methods* **12**, 859–865 (2015).
9. E. M. Huber et al., *Cell* **148**, 727–738 (2012).
10. E. M. Huber et al., *Nat. Commun.* **7**, 10900 (2016).
11. E. M. Huber, W. Heinemeyer, M. Groll, *Structure* **23**, 407–417 (2015).
12. S. D. Demo et al., *Cancer Res.* **67**, 6383–6391 (2007).
13. T. A. Grigoreva, V. G. Tribulovich, A. V. Garabadzhiu, G. Melino, N. A. Barlev, *Oncotarget* **6**, 24733–24749 (2015).
14. M. Groll, K. B. Kim, N. Kairies, R. Huber, C. M. Crews, *J. Am. Chem. Soc.* **122**, 1237–1238 (2000).
15. J. F. Lynas, P. Harriott, A. Healy, M. A. McKervey, B. Walker, *Bioorg. Med. Chem. Lett.* **8**, 373–378 (1998).
16. M. A. Gräwert et al., *Angew. Chem. Int. Ed. Engl.* **50**, 542–544 (2011).
17. R. C. Kane, A. T. Farrell, R. Sridhara, R. Pazdur, *Clin. Cancer Res.* **12**, 2955–2960 (2006).
18. M. Shirley, *Drugs* **76**, 405–411 (2016).
19. M. K. Bennett, C. J. Kirk, *Curr. Opin. Drug Discov. Devel.* **11**, 616–625 (2008).

MOLECULAR IMAGING

Spatial organization of chromatin domains and compartments in single chromosomes

Siyuan Wang,[1] Jun-Han Su,[1] Brian J. Beliveau,[2]* Bogdan Bintu,[1] Jeffrey R. Moffitt,[1] Chao-ting Wu,[2]† Xiaowei Zhuang[1]†

The spatial organization of chromatin critically affects genome function. Recent chromosome-conformation-capture studies have revealed topologically associating domains (TADs) as a conserved feature of chromatin organization, but how TADs are spatially organized in individual chromosomes remains unknown. Here, we developed an imaging method for mapping the spatial positions of numerous genomic regions along individual chromosomes and traced the positions of TADs in human interphase autosomes and X chromosomes. We observed that chromosome folding deviates from the ideal fractal-globule model at large length scales and that TADs are largely organized into two compartments spatially arranged in a polarized manner in individual chromosomes. Active and inactive X chromosomes adopt different folding and compartmentalization configurations. These results suggest that the spatial organization of chromatin domains can change in response to regulation.

The spatial organization of chromatin, such as chromatin domains, chromatin loops, associations of chromatin with nuclear structures, and chromosome territories, plays an important role in essential genome functions (*1–6*). However, many gaps remain in our understanding of the three-dimensional (3D) folding of individual chromosomes in the nucleus. Recently, chromosome-conformation-capture methods such as Hi-C (*4, 7*) have revealed a wealth of structural insights for interphase chromosomes. For example, chromatin is organized into topologically associating domains (TADs) or contact domains that are hundreds of kilobases (kb) in size (*8–11*). These domains tend to spatially segregate from each other (*9, 12, 13*) and, in *Drosophila*, correspond to the banding patterns of polytene chromosomes (*14, 15*). At length scales from several hundred kilobases to several megabases, the power-law scaling of Hi-C contact frequency is consistent with a fractal-globule polymer model (*7, 16*), whereas, within TADs, Hi-C contact maps are better described by a loop-extrusion model (*17, 18*). Superresolution imaging shows that chromatin domains in different epigenetic states adopt distinct folding configurations with different power-law scaling properties (*13*). Whether the ideal fractal-globule model can describe chromatin at length scales be-yond several megabases remains an open question (*19, 20*). Hi-C analyses have also revealed two multi-TAD compartments, compartments A and B, that are enriched with active and inactive chromatin, respectively (*7, 21*). However, because the contact maps used to identify these compartments were derived from ensemble averaging of many chromosomes, it is unclear whether the A and B compartments are structures that exist in individual chromosomes inside single cells and, if so, how the two compartments are spatially arranged with respect to each other. To answer questions regarding the spatial organization of individual chromosomes requires methods that directly visualize the conformation of single chromosomes in single cells.

Fluorescence in situ hybridization (FISH) provides a powerful means to directly image the spatial organization of chromosomes, especially when used to simultaneously target two or more genomic loci (e.g., *19, 20, 22–24*). In one effort, a three-color barcoding approach has been used to simultaneously label multiple chromatin loci to trace the conformation of a chromosome arm in *Drosophila* blastoderm embryos (*24*). Nonetheless, routine tracing of the complex 3D folding path of chromosomes has remained challenging because of the difficulties associated with simultaneously imaging and unambiguously identifying many genomic regions on interphase chromosomes. Here, we report a multiplexed FISH method that enables sequential imaging of many genomic regions for 3D tracing of individual chromosomes in the nucleus and the use of this method to study the spatial arrangements of TADs and compartments in chromosomes 20, 21, 22, and X of human diploid (XX) IMR90 cells.

[1]Howard Hughes Medical Institute, Department of Chemistry and Chemical Biology, Department of Physics, Harvard University, Cambridge, MA 02138, USA. [2]Department of Genetics, Harvard Medical School, Boston, MA 02115, USA.
*Present address: Wyss Institute for Biologically Inspired Engineering, Harvard University, Boston, MA 02446, USA.
†Corresponding author. Email: zhuang@chemistry.harvard.edu (X.Z.); twu@genetics.med.harvard.edu (C.-t.W.)

Fig. 1. Mapping the spatial organization of the central 100-kb regions of all 34 TADs in chromosome 21 (Chr21) of IMR90 cells. (**A**) A simplified scheme of the imaging approach. All primary probes are first hybridized to the targeted chromosome, after which secondary probes targeting each TAD are sequentially hybridized to the readout sequences on the primary probes, imaged, and then bleached. In each round of secondary hybridization, two different secondary probes tagged with dyes of different colors allowed simultaneous visualization of two TADs. More details are depicted in fig. S1. (**B**) Image of an IMR90 cell after the primary hybridization (Hyb 0) with primary probes targeting all TADs in Chr21. The two bright patches, one marked by a yellow box, correspond to the two copies of Chr21 in this diploid cell. (**C**) Images of the yellow-boxed region in (B) after each round of secondary hybridization (Hyb 1 to 17). (**D**) Positions of the 34 TADs of the chromosome were plotted as red dots overlaid on the Hyb 0 image. Scale bars in (B) to (D), 2 μm. (**E**) TAD positions plotted in 3D. (**F**) Mean spatial distance matrix for the 34 TADs, with each element of the matrix corresponding to the mean spatial distance between a pair of TADs. (**G**) Inverse Hi-C contact frequency between each pair of TADs versus their mean spatial distance. The correlation coefficient (R) and the slope of a fitted line (k) are shown. Contact frequency is calculated as the total Hi-C counts between two TADs normalized to their genomic lengths (8). (**H**) Mean spatial distance versus genomic distance for all pairs of TADs. The lines are power-law function fits with either a predefined scaling exponent ($S = 1/3$, green) or with S as a fitting parameter (red). Data from 120 individual chromosomes were used to generate (F) to (H).
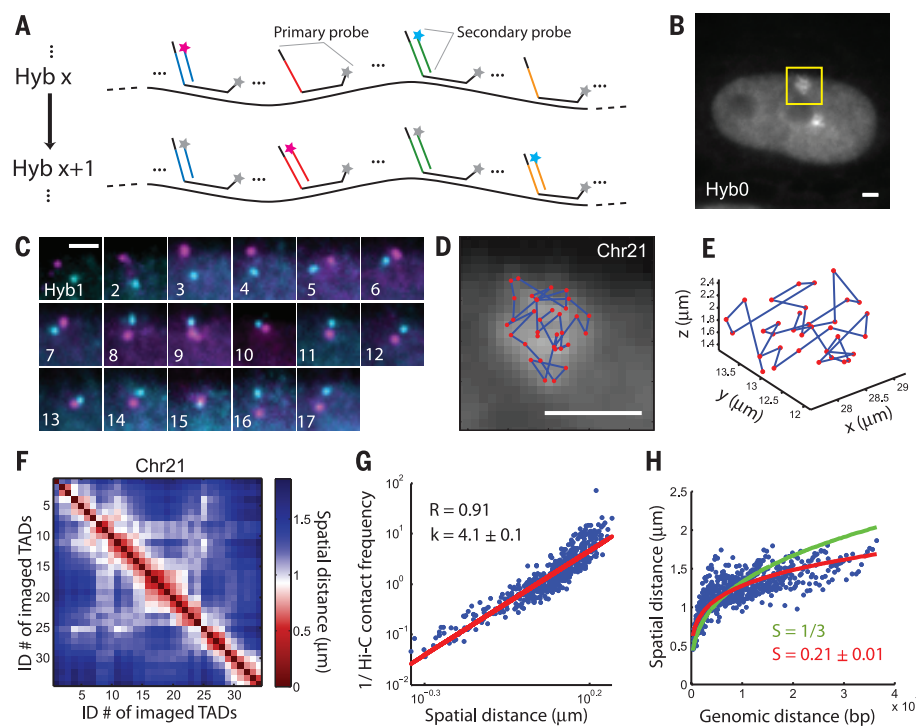
To map the 3D spatial positions of TADs, delineated here as genomic domains based on ensemble-average Hi-C maps (8), along an entire chromosome, we labeled the central 100-kb regions of TADs using a dual-oligonucleotide version of Oligopaints (25, 26), wherein each TAD was targeted with 1000 distinct "primary" oligonucleotide probes and a companion "secondary" probe (Fig. 1A and fig. S1). Each of the 1000 primary probes consisted of a unique targeting sequence complementary to a given sequence within the TAD and a nongenomic region, called Mainstreet, that contained a readout sequence shared by all 1000 probes but unique for each TAD. The secondary probe contained a sequence complementary to the readout sequence on Mainstreet. We used the genomic coordinates of TADs derived from Hi-C (8) to design the targeting sequences of primary probes and produced these probes with a high-yield enzymatic amplification method (27). We exploited a similar hybridization and imaging protocol as we previously described in multiplexed error-robust fluorescence in situ hybridization (MERFISH) (27) but with some modifications. First, we hybridized all primary probes to the chromosome of interest (fig. S1, Hyb 0), imaged the sample, and located the chromosome in the nucleus. We then photobleached the sample and performed a series of secondary hybridizations, separated by photobleaching, to sequentially label and image individual TADs (Fig. 1A and fig. S1, Hyb 1, Hyb 2, and so on). Each round

of secondary hybridization employed two different secondary probes, respectively labeled with two spectrally distinct dyes, enabling us to visualize two TADs simultaneously using two-color, 3D fluorescence imaging with z-stepping. The centroid positions of the 3D images of individual TADs were used to approximate their positions in x, y, and z.

We first used this method to image chromosome 21 (Chr21) in interphase IMR90 cells. The Hyb 0 image showed that, when imaged together, the fluorescent signals from all 34 TADs of Chr21 coalesced into a continuous patch (Fig. 1B). The 17 rounds of secondary hybridization then allowed us to image each of the 34 TADs separately (Fig. 1C), determine the 3D position of each TAD, and trace the 3D path of this chromosome at the TAD level (Fig. 1, D and E). To characterize the organization of Chr21, we traced 120 copies of Chr21 in many cells, calculated the mean spatial distance between each pair of TADs (averaged over all 120 chromosomes), and constructed a pair-wise mean spatial distance matrix for the 34 TADs (Fig. 1F).

To compare our measurements with previous Hi-C data (8), we correlated the mean spatial distance matrix with the corresponding Hi-C contact frequency matrix of Chr21 (fig. S2). Notably, the mean spatial distance showed high correlation with the inverse contact frequency between TADs, with a Pearson correlation coefficient of 0.91 across nearly

three orders of magnitude in contact frequency (Fig. 1G). Such a strong correlation between the results from two different methods provided a cross validation for both methods at the TAD-to-chromosome length scales probed in this work. The relationship between the spatial distance and contact frequency also provides a valuable measure for exploring chromosome organization. A mean-field approximation predicts that the contact frequency should be inversely proportional to the third power of the mean spatial distance, whereas the power for real chromatin is expected to be bigger than 3 (19). Our data showed that the Hi-C contact frequency was inversely proportional to the fourth power of the mean spatial distance [Fig. 1G, scaling exponent $k = 4.1 \pm 0.1$, 95% confidence interval (CI), $N = 120$ chromosomes]. We also analyzed the distributions of the spatial distances between pairs of TADs (fig. S3) and found that the Hi-C contact frequency scaled linearly with the probability of two TADs coming into spatial proximity (fig. S4). These results suggest a calibration function to convert Hi-C contact frequencies into mean spatial distances at TAD-to-chromosome length scales, although it remains to be determined whether this calibration extends to sub-TAD scales where the correlation between the Hi-C contact frequency and spatial proximity may be weaker (28).

In addition, our data showed that the mean spatial distance between TADs scaled with

Fig. 2. Spatial organization of compartments in individual chromosomes of Chr21. (**A**) Normalized spatial distance matrix for the 34 TADs, normalized over the expected spatial distances determined by the power-law function fit in Fig. 1H (red line). (**B**) Pearson correlation matrix of the 34 TADs, determined from the normalized spatial distance matrix in (A). (**C**) Pearson correlation matrix of the 34 TADs calculated from previous Hi-C data (8). (**D**) Assignment of TADs to compartment A (red bars) or compartment B (blue bars) based on a principal components analysis of the Pearson correlation matrix shown in (B). (**E**) (Left panels) Spatial position maps of compartment-A TADs (red) and compartment-B TADs (blue) in two individual chromosomes. For better visualization, the chromosomes were rotated so that the polarization axis connecting the centroids of compartments A and B is aligned along the z axis. (Right panels) Corresponding 3D convex hull plots. (**F**) Polarization index values measured for individual chromosomes (observed) in comparison with those derived from a randomization

control where the compartment assignments were randomized while maintaining the total number of TADs in each compartment. The nonzero control values arose from fluctuations associated with the finite number of TADs per chromosome, which provides a baseline for comparison. Each dot corresponds to the polarization index of a single chromosome, the red lines represent the median values, and the blue boxes represent the 25% to 75% quantiles. **P < 0.001 (Wilcoxon test). Data from 120 individual chromosomes were used to generate (A), (B), (D), and (F).
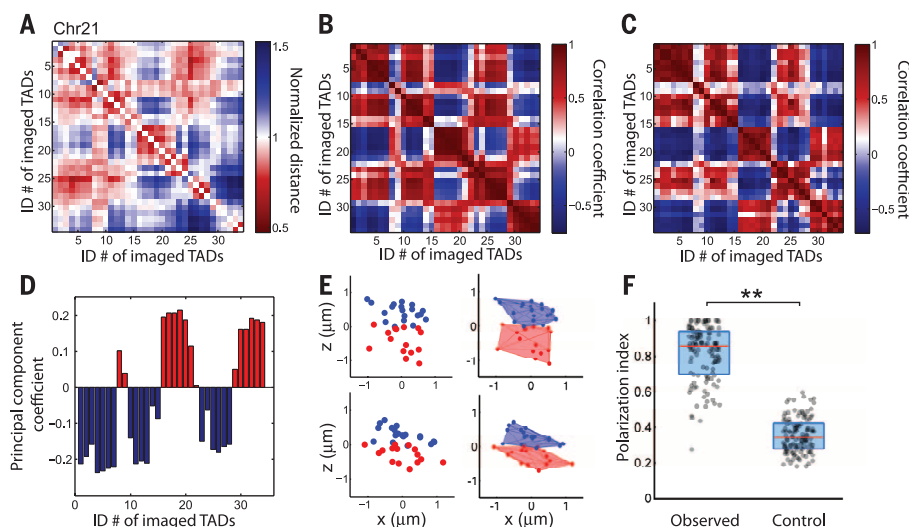
their genomic distance to about one-fifth power (Fig. 1H, scaling exponent $S = 0.21 \pm 0.01$, 95% CI, $N = 120$ chromosomes). This value deviated from the one-third power expected from the ideal fractal-globule polymer model (19). The deviation was most pronounced for large genomic distances, whereas data points with genomic distances less than 7 Mb showed a scaling exponent close to one-third (fig. S5), consistent with previous results (7, 19). Interestingly, a previous simulation of confined, unknotted, finite-sized polymers showed a deviation of the scaling exponent from one-third at large length scales (29), suggesting a possible physical model to explain our experimental observation.

Next, we determined whether the spatial positions of TADs are partitioned into distinct compartments by implementing a normalization analysis similar to that performed for the Hi-C data (7). First, we normalized the mean spatial distance matrix to the expected spatial distance at each genomic distance as predicted by the power-law scaling shown in Fig. 1H. The normalized spatial distance matrix showed a pattern with alternating regions of large and small values (Fig. 2A), suggesting the existence of two subgroups of TADs. Next, we calculated the Pearson correlation coefficient between each pair of columns in the normalized distance matrix, defined this coefficient as the correlation between the two corresponding TADs, and constructed a Pearson correlation matrix for all TAD pairs (Fig. 2B). This Pearson correlation matrix showed a plaid pattern, consistent with the existence of two compartments with TADs from the same compartment being positively correlated. For comparison, we used a similar approach (7)

to analyze the Hi-C data (8) and obtained a nearly identical Pearson correlation matrix (Fig. 2C), suggesting that the two compartments observed in our imaging data correspond to the A and B compartments identified by Hi-C analysis (7, 21). To assign each TAD to a compartment, we performed a principal components analysis on the Pearson correlation matrix derived from the normalized spatial distances and assigned TADs with positive and negative values along the first principal component to compartments A and B, respectively (Fig. 2D). Nearly identical assignment was obtained by applying the principal components analysis directly to the normalized spatial distance matrix (fig. S6). We further observed that histone modifications for active chromatin (30, 31) and inactive chromatin (32) were enriched in compartments A and B, respectively (fig. S7), consistent with previous Hi-C analysis (7). We then analyzed the scaling relationship between inverse Hi-C contact frequency and mean spatial distance for pairs of TADs that are either within the same compartment or cross-compartment and found that cross-compartment TAD pairs gave a moderately higher scaling exponent (fig. S8).

The above population-averaged analyses cannot reveal whether the higher correlation observed between TADs in the same compartment represents transient proximity between these TADs or whether the two compartments are physical structures that exist in individual chromosomes, nor can they reveal how compartments are spatially arranged—e.g., whether one compartment wraps around the other to form a radial organization within a single chromosome or whether the two compart-

ments are arranged in a side-by-side, polarized manner. To address these questions, we examined the spatial positions of the central regions of TADs in single chromosomes. Notably, most individual chromosomes in single cells showed a spatially polarized arrangement of compartment-A and compartment-B TADs (Fig. 2E). To quantify the polarized separation of the compartments in individual chromosomes, we defined a polarization index as $\sqrt{(1-V_S/V_A)(1-V_S/V_B)}$, where V_A and V_B are the convex hull volumes of the two compartments and V_S is their shared volume. If the two compartments perfectly overlap with each other, or if one compartment wraps around the other, the polarization index should equal zero; on the other hand, if the two compartments are completely separated in space in a polarized manner, the polarization index should equal 1 (fig. S9). The measured polarization index values of Chr21 were indeed close to 1, with a median value of 0.86, substantially larger than the values derived from a randomization control (Fig. 2F).

To investigate whether the above findings were chromosome-specific, we traced the positions of the central 100-kb regions of TADs in Chr22 and Chr20 by imaging all 27 TADs in Chr22 and 30 of the 60 TADs (every other one) in Chr20 and found conclusions similar to those described for Chr21. First, the Hi-C contact frequency was inversely proportional to the fourth power of the mean spatial distance between TADs (figs. S10A and S11A). Second, the mean spatial distance between TADs scaled with genomic distance to a similar, albeit slightly smaller, power than in Chr21 (Fig. 3, A and B), substantially deviating from the one-third power predicted by the
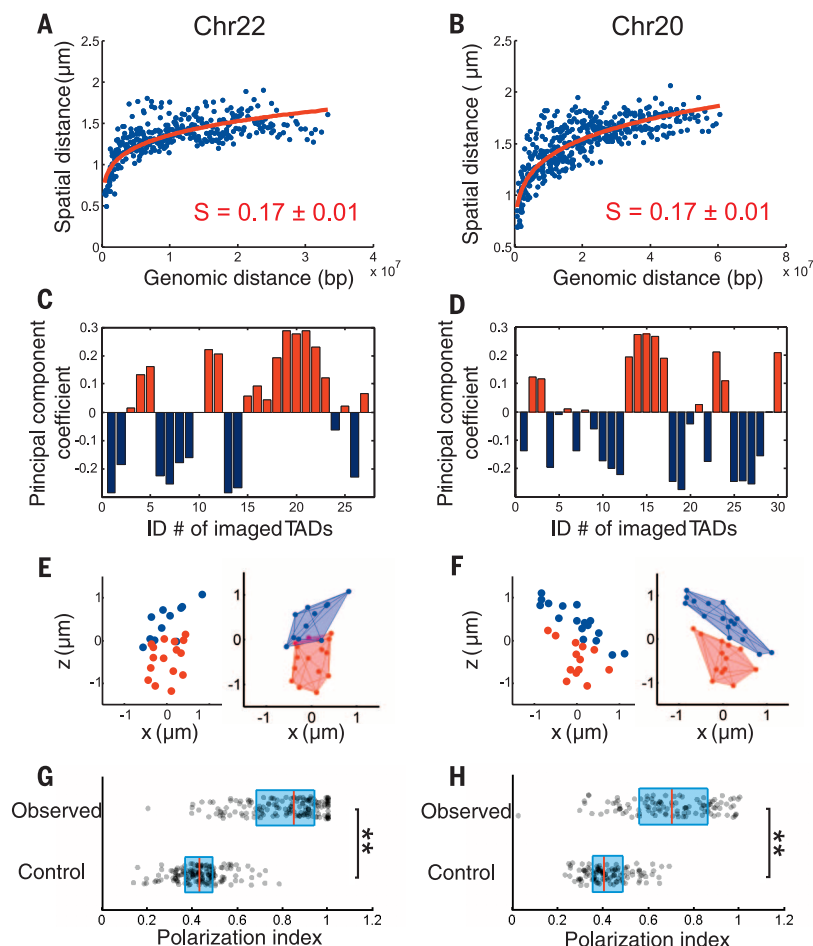
Fig. 3. Spatial organization of the central 100-kb regions of TADs in chromosome 22 (Chr22) and chromosome 20 (Chr20). (**A** and **B**) Mean spatial distance versus genomic distance for Chr22 (A) and Chr20 (B). Power-law function fits are shown as red lines, and the scaling exponents (S) are shown. (**C** and **D**) Compartment assignments of TADs based on principal components analyses of the Pearson correlation matrix for Chr22 (fig. S10D) and Chr20 (fig. S11D). Blue bars, compartment B. Red bars, compartment A. (**E** and **F**) Spatial position maps of compartment-A TADs (red) and compartment-B TADs (blue) in single chromosomes for Chr22 (E) and Chr20 (F), plotted without (left) or with (right) 3D convex hulls. (**G** and **H**) Polarization index values measured for individual chromosomes for Chr22 (G) and Chr20 (H) (observed) in comparison with those of the randomization control (control). The dots, red lines, and blue boxes are defined as in Fig. 2F. **$P < 0.001$ (Wilcoxon test). Data from ~150 individual chromosomes were used to generate (A), (C), and (G), and data from ~110 individual chromosomes were used to generate (B), (D), and (H).

ideal fractal-globule model. Third, analysis based on spatial distances showed that TADs in Chr22 and Chr20 were partitioned into two spatial compartments (Fig. 3, C and D, and figs. S10, B to E, and S11, B to E), with assignments nearly identical to those obtained from our analysis on Hi-C data. These two compartments were again spatially organized in a polarized, side-by-side manner in individual chromosomes (Fig. 3, E to H), although the degree of polarized separation is moderately smaller in Chr20. Whether these findings extend to all other autosomes remains to be determined.

Finally, we traced the positions of the central 100-kb regions of TADs in the X chromosome (ChrX). We imaged 40 TADs (out of 86 total) spanning the whole chromosome at relatively uniform intervals. It is known that one of the two copies of ChrX in female mammalian cells undergoes X-inactivation (33, 34). We used TAD coordinates obtained from the combined Hi-C data (8) of both active and inactive copies of ChrX (Xa and Xi) to determine labeling sites but note that the TAD structures are attenuated or absent on Xi (9, 35). We distinguished Xa and Xi by immunostaining of macroH2A.1 (fig. S12), a histone variant enriched in Xi (35). The mean spatial distance matrices of Xi and Xa were strikingly different, with the Xi matrix elements being substantially more homogeneous and mostly having smaller values than the Xa matrix elements (fig. S13, A and B). Indeed, fitting a power-law function to the spatial versus genomic distance plot yielded a very small scaling exponent of $S = 0.074 \pm 0.003$ (95% CI, $N = 95$ chromosomes) for Xi (Fig. 4A), whereas the scaling exponent for Xa ($S = 0.22 \pm 0.01$, 95% CI, $N = 95$ chromosomes) remained similar to those of Chr20, Chr21, and Chr22 (Fig. 4B). These observations suggest that Xi not only was more compact (36) but also adopted a spatially more intermixed chromatin arrangement with more homogeneous interloci distances, reminiscent of the chromatin organization observed for Polycomb-repressed domains using superresolution imaging (13). Given the enrichment of Polycomb group proteins on Xi (33, 34), these observations suggest a potentially general mechanism to induce such a compact and highly intermixed chromatin folding configuration.

Notably, ChrX also formed two compartments, but the compartmentalization schemes were different for Xi and Xa. Consistent with previous allele-specific Hi-C analyses (21, 35, 37), Xi was largely partitioned into two contiguous compartments (also called superdomains or megadomains) separated on the genomic map by the DXZ4 macrosatellite (Fig. 4C and fig. S13, C, E, and G). Such a scheme might result from the ability of the DXZ4 element to recruit the chromatin insulator CTCF to Xi but not to Xa (38). The Xa TADs were also partitioned into two spatial compartments, but the two compartments corresponded instead to the p and q arms of the chromosome (Fig. 4D and fig. S13, D, F, and H). Interestingly, the two compartments in both Xa and Xi were again spatially organized in a polarized, side-by-side manner in individual chromosomes (Fig. 4, E to H). However, the degree of polarized segregation was notably smaller for Xi (Fig. 4G), consistent with our observation of more intermixed chromatin in Xi. It is worth noting that within the individual arms of Xa, TADs were further partitioned into two subcompartments (fig. S14, A to C), one of which appeared to be relatively enriched with histone modifications for active chromatin (fig. S14D), implying that these subcompartments potentially correspond to the A and B compartments.

Our observation that compartments A and B are organized in a spatially polarized manner in single chromosomes in most cells suggests that these are relatively stable physical structures that are present most of the time in individual cells. The fact that we observed this spatial organization for all three examined autosomes (Chr20, 21, and 22) also supports the possibility that these structures are functionally important and maintained by specific mechanisms (2, 4). Because compartments A and B consist mainly of active and inactive chromatin, respectively (7, 21), their presence may serve to locally enrich for transcription
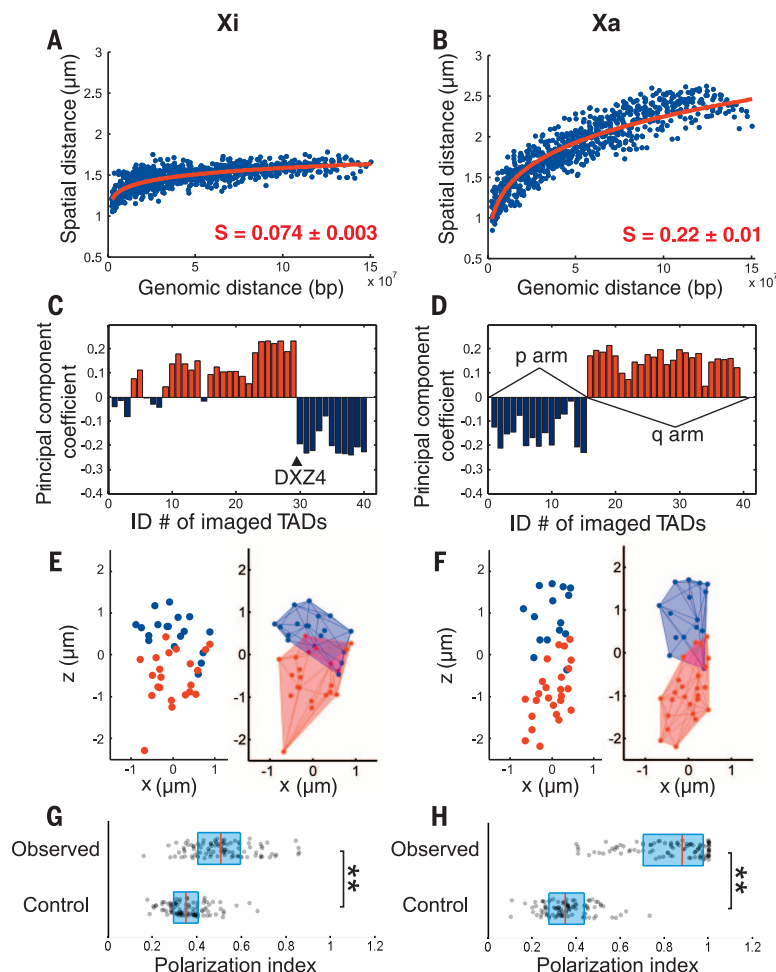
Fig. 4. Spatial organization of the central 100-kb regions of TADs in inactive and active X (Xi and Xa) chromosomes. The TAD structures are attenuated or absent on Xi (9, 35) and hence, for Xi, the term "TAD" simply represents imaged genomic loci. (**A** and **B**) Mean spatial distance versus genomic distance for Xi (A) and Xa (B). Power-law function fits are shown as red lines, and the scaling exponents (S) are shown. (**C** and **D**) Compartment assignments for Xi (C) and Xa (D), based on principal components analyses of the Pearson correlation matrix for Xi (fig. S13C) and Xa (fig. S13D). Positions of the DXZ4 macrosatellite in Xi and the p and q arms in Xa are indicated. (**E** and **F**) Spatial position maps of TADs in single Xi (E) and Xa (F) chromosomes, without (left) or with (right) 3D convex hulls. (**G** and **H**) Polarization index measured for Xi (G) and Xa (H) (observed) in comparison with those of the randomization control (control). The dots, red lines, and blue boxes are defined as in Fig. 2F. **P < 0.001 (Wilcoxon test). Data from 95 individual chromosomes were used to generate (A) to (D), (G), and (H).

machinery and/or epigenetic regulators and thus enhance the efficient use of these molecular resources. The interactions that maintain these compartments could be direct and/or indirect—i.e., some chromatin binding factors may directly cross-link TADs belonging to the same compartment or some factors may recruit TADs to predefined nuclear areas to form compartments. The large-scale extension of chromatin upon activation (39, 40) may also contribute to the separation of inactive and active chromatin. Finally, we observed distinct compartmentalization schemes for inactive and active X chromosomes, with Xi being partitioned into two contiguous compartments separated by

the DXZ4 element (21, 35, 37) and Xa being partitioned according to the p and q arms, although individual arms of Xa may be further partitioned into A and B compartments. Together, these results suggest that the spatial organization of chromatin domains may play an important role in gene regulation and that this organization could be altered to facilitate different chromosomal functions.

REFERENCES AND NOTES

1. T. Misteli, *Cell* **128**, 787–800 (2007).
2. D. U. Gorkin, D. Leung, B. Ren, *Cell Stem Cell* **14**, 762–775 (2014).
3. M. Levine, C. Cattoglio, R. Tjian, *Cell* **157**, 13–25 (2014).
4. J. Dekker, L. Mirny, *Cell* **164**, 1110–1121 (2016).
5. W. A. Bickmore, B. van Steensel, *Cell* **152**, 1270–1284 (2013).
6. T. Cremer, M. Cremer, *Cold Spring Harb. Perspect. Biol.* **2**, a003889 (2010).
7. E. Lieberman-Aiden et al., *Science* **326**, 289–293 (2009).
8. J. R. Dixon et al., *Nature* **485**, 376–380 (2012).
9. E. P. Nora et al., *Nature* **485**, 381–385 (2012).
10. T. Sexton et al., *Cell* **148**, 458–472 (2012).
11. C. Hou, L. Li, Z. S. Qin, V. G. Corces, *Mol. Cell* **48**, 471–484 (2012).
12. P. J. Fabre et al., *Proc. Natl. Acad. Sci. U.S.A.* **112**, 13964–13969 (2015).
13. A. N. Boettiger et al., *Nature* **529**, 418–422 (2016).
14. K. P. Eagen, T. A. Hartl, R. D. Kornberg, *Cell* **163**, 934–946 (2015).
15. S. V. Ulianov et al., *Genome Res.* **26**, 70–84 (2016).
16. L. A. Mirny, *Chromosome Res.* **19**, 37–51 (2011).
17. G. Fudenberg et al., *Cell Reports* **15**, 2038–2049 (2016).
18. A. L. Sanborn et al., *Proc. Natl. Acad. Sci. U.S.A.* **112**, E6456–E6465 (2015).
19. J. D. Halverson, J. Smrek, K. Kremer, A. Y. Grosberg, *Rep. Prog. Phys.* **77**, 022601 (2014).
20. J. Mateos-Langerak et al., *Proc. Natl. Acad. Sci. U.S.A.* **106**, 3812–3817 (2009).
21. S. S. P. S. P. Rao et al., *Cell* **159**, 1665–1680 (2014).
22. H. Yokota, G. van den Engh, J. E. Hearst, R. K. Sachs, B. J. Trask, *J. Cell Biol.* **130**, 1239–1249 (1995).
23. K. Bystricky, P. Heun, L. Gehlen, J. Langowski, S. M. Gasser, *Proc. Natl. Acad. Sci. U.S.A.* **101**, 16495–16500 (2004).
24. M. G. Lowenstein, T. D. Goddard, J. W. Sedat, *Mol. Biol. Cell* **15**, 5678–5692 (2004).
25. B. J. Beliveau et al., *Proc. Natl. Acad. Sci. U.S.A.* **109**, 21301–21306 (2012).
26. B. J. Beliveau et al., *Nat. Commun.* **6**, 7147 (2015).
27. K. H. Chen, A. N. Boettiger, J. R. Moffitt, S. Wang, X. Zhuang, *Science* **348**, aaa6090 (2015).
28. I. Williamson et al., *Genes Dev.* **28**, 2778–2791 (2014).
29. M. V. Imakaev, K. M. Tchourine, S. K. Nechaev, L. A. Mirny, *Soft Matter* **11**, 665–671 (2015).
30. R. D. Hawkins et al., *Cell Stem Cell* **6**, 479–491 (2010).
31. B. E. Bernstein et al., *Nat. Biotechnol.* **28**, 1045–1048 (2010).
32. T. Chandra et al., *Mol. Cell* **47**, 203–214 (2012).
33. D. Lessing, M. C. Anguera, J. T. Lee, *Annu. Rev. Genomics Hum. Genet.* **14**, 85–110 (2013).
34. R. Galupa, E. Heard, *Curr. Opin. Genet. Dev.* **31**, 57–66 (2015).
35. A. Minajigi et al., *Science* **349**, aab2276 (2015).
36. C. Naughton, D. Sproul, C. Hamilton, N. Gilbert, *Mol. Cell* **40**, 397–409 (2010).
37. X. Deng et al., *Genome Biol.* **16**, 152 (2015).
38. A. H. Horakova, S. C. Moseley, C. R. McLaughlin, D. C. Tremblay, B. P. Chadwick, *Hum. Mol. Genet.* **21**, 4367–4377 (2012).
39. T. Tumbar, G. Sudlow, A. S. Belmont, *J. Cell Biol.* **145**, 1341–1354 (1999).
40. M. J. Levesque, A. Raj, *Nat. Methods* **10**, 246–248 (2013).

Science

Spatial organization of chromatin domains and compartments in single chromosomes

Siyuan Wang, Jun-Han Su, Brian J. Beliveau, Bogdan Bintu, Jeffrey R. Moffitt, Chao-ting Wu and Xiaowei Zhuang

Spatial organization inside the nucleus

In eukaryotic cells, DNA is packaged into a complex macromolecular structure called chromatin. Wang *et al.* have developed an imaging method to map the position of multiple regions on individual chromosomes, and the results confirm that chromatin is organized into large contact domains called TADS (topologically associating domains). Unexpectedly, though, folding deviates from the classical fractal-globule model at large length scales.

Science, this issue p. 598

ARTICLE TOOLS	http://science.sciencemag.org/content/353/6299/598
SUPPLEMENTARY MATERIALS	http://science.sciencemag.org/content/suppl/2016/07/20/science.aaf8084.DC1
REFERENCES	This article cites 51 articles, 15 of which you can access for free http://science.sciencemag.org/content/353/6299/598#BIBL
PERMISSIONS	http://www.sciencemag.org/help/reprints-and-permissions

Use of this article is subject to the Terms of Service